INDI Control Techniques and Automatic Landing Procedures

Salma Abass

Bachelorarbeit

2023

Universität Stuttgart
Institut für Flugmechanik und Flugregelung

Declaration

Hiermit versichere ich, dass ich diese Bachelorarbeit selbständig mit Unterstützung der Betreuer angefertigt und keine anderen als die angegebenen Quellen und Hilfsmittel verwendet habe.

Die Arbeit oder wesentliche Bestandteile davon sind weder an dieser noch an einer anderen Bildungseinrichtung bereits zur Erlangung eines Abschlusses eingereicht worden.

Ich erkläre weiterhin, bei der Erstellung der Arbeit die einschlägigen Bestimmungen zum Urheberschutz fremder Beiträge entsprechend den Regeln guter wissenschaftlicher Praxis[1] eingehalten zu haben. Soweit meine Arbeit fremde Beiträge (z.B. in der Form von Bildern, Zeichnungen, Textpassagen etc.) enthält, habe ich diese Beiträge als solche gekennzeichnet (Zitat, Quellenangabe) und eventuell erforderlich gewordene Zustimmungen der Urheber zur Nutzung dieser Beiträge in meiner Arbeit eingeholt. Mir ist bekannt, dass ich im Fall einer schuldhaften Verletzung dieser Pflichten die daraus entstehenden Konsequenzen zu tragen habe.

Ort, Datum	Salma Abass

Betreuer: Prof.Dr.-Ing. Walter Fichter

[1] Nachzulesen in den DFG-Empfehlungen zur „Sicherung guter wissenschaftlicher Praxis“ bzw. in der Satzung der Universität Stuttgart zur “Sicherung der Integrität wissenschaftlicher Praxis und zum Umgang mit Fehlverhalten in der Wissenschaft“

Abstract

This research focuses on automated aircraft operations during landing using Incremental Nonlinear Dynamic Inversion (INDI) control for a fixed-wing tricycle gear UAV. The paper highlights the challenges in automating the aircraft operations due to model uncertainties and ground effect. The control architecture comprises four loops, with INDI applied to flight path and angular rate control loops. The results demonstrate successful INDI-based flight controller implementation, improving robustness and maneuver accuracy in low-altitude flight. The future work includes validation through Hardware-in-the-loop simulations and flight tests to enhance the control system's performance and enable real-world application.

Contents

List of Figures

Nomenclature

Abbreviations

ATOL	Automatic Takeoff and Landing
DOF	Degree(s) of Freedom
GNC	Guidance, Navigation, and Control
INDI	Incremental Nonlinear Dynamic Inversion
NDI	Nonlinear Dynamic Inversion
UAV	Unmanned Aerial Vehicle

Latin letters

$(\mathrm{C}_D\ C_Q\ C_L)^T$	$[-]$	Aerodynamic Force coefficients
$(\mathrm{C}_l\ C_m\ C_n)^T$	$[-]$	Aerodynamic moment coefficients
b	$[m]$	Wing span
c	$[m]$	Mean aerodynamic chord
g	$[\mathrm{m/s}^2]$	Gravitational acceleration
m	$[Kg]$	Aircraft mass
q	$[N/m]$	Dynamic pressure
S	$[\mathrm{m}^2$	Wing surface area
V_A	$[m/s]$	velocity of aircraft wrt the air
V_k	$[m/s]$	velocity of aircraft wrt the ground
V_w	$[m/s]$	Velocity of air wrt the ground

Greek letters

$(\mu\ \alpha\ \beta)^T$	Attitude angles wrt. aerodynamic frame
$(\phi\ \theta\ \psi)^T$	Euler angles
$(\xi\ \eta\ \zeta)^T$	Control surfaces: aileron, elevator, rudder
$(p\ q\ r)^T$	Angular velocity vector in body frame
χ	Azimuth
γ	Flight path angle
ρ	Air density

1 Introduction

In recent years, the field of unmanned aerial vehicles (UAVs) has witnessed remarkable advancements, enabling a wide range of applications across industries. Among these UAVs, fixed-wing tricycle gear UAVs have gained considerable popularity due to their ability to cover long distances efficiently and their versatility in various mission scenarios. Unlike rotary-wing UAVs, such as quadcopters or helicopters, which rely on rotating blades to generate lift and maneuver, fixed-wing UAVs have wings that provide the necessary lift for sustained flight. These wings are fixed in position and typically resemble those of traditional manned aircraft. Furthermore, tricycle gear refers to the arrangement of landing gear, where the plane has one forward-facing wheel under the nose and two main wheels under the wings. This configuration offers stability and control during ground operations.

As the demand for UAV operations continues to grow, there is a pressing need to improve their operational efficiency, reliability, and safety. One of the crucial elements of UAV operations is the process of takeoff and landing, which has traditionally relied on human intervention and piloting expertise. However, as UAV technology continues to evolve, there is a growing emphasis on automating these procedures to enhance operational efficiency and reduce the potential for human error. This is particularly important in scenarios where UAVs are required to perform repetitive missions or operate in challenging environments where manual control may be impractical or unsafe. This automation can also lead to increased operational capacity by reducing the time required for each flight and allowing for more efficient utilization of UAVs.

The implementation of ATOL (Automatic Takeoff and Landing) functionality presents several challenges that must be taken into account when designing the control system. Due to the increased vulnerability of light aircraft to environmental factors such as wind and ground effects, the control effort required to track the desired states accurately becomes more demanding. A vital factor to take into account is the availability of aircraft models for controller development. Obtaining precise models for light aircrafts is exceptionally challenging, often resulting in significant uncertainties that necessitate the robustness of the control systems. Generally, it can be asserted that the conventional approach to control design is not well-suited to address the challenges mentioned earlier, particularly in the presence of ground effect. Furthermore, an additional challenge arises during the flare phase of the landing process. During this phase, the aircraft undergoes rotation around its lateral axis to elevate its path inclination and pitch angle. This maneuver presents conflicting control objectives concerning θ (path inclination), γ (pitch angle), and V_A (airspeed), which have significant implications at this particular stage.

The successful management of this over-actuated system relies on effectively leveraging the interdependence among all three states, as will be discussed later.

In this context, this paper aims to explore the application of the Incremental Nonlinear Dynamic Inversion (INDI) protocol in automating the takeoff and landing procedures of UAVs.This control strategy offers significant advantages, primarily through reduced reliance on the aircraft model. Instead of relying on precise models, INDI utilizes translational and rotational accelerations measurements, which account for all non-linearities and eliminate potential model uncertainties. A control architecture comprising four loops has been developed, encompassing position control, flight path control, attitude control, and angular rate control. After careful analysis, it has been determined that model uncertainties only affect the flight path and angular rate control loops. Consequently, the INDI control law is utilized to design these two control loops, while the remaining two are designed using the NDI control law.

The structure of this paper is as follows: chapter 2 provides essential background information and explains the basic theory and principles of INDI as well as the reason of its selection. In chapter 3, the aircraft model which is used to design the controller is introduced and then the control structure is derived and implemented on Simulink. Chapter 4 outlines the testing setup, simulation results, and conclusion. Finally, chapter 5 provides a summary and outlines possible future work.

2 Background

2.1 Coordinate systems

Several coordinate systems are defined to clarify the derivation of the equations of motion. In every coordinate system that moves with the airplane, the x and z axes are situated in the airplane's symmetry plane, whereas the y-axis is placed in a right-handed manner. The x-axis aligns with the airplane's motion, while the z-axis points towards the earth if the aircraft is upright. The following four coordinate systems are utilized (refer to Fig2.1)

1. The ground axes system E_{xyz} is fixed to the Earth's surface at mean sea level. It is assumed that the Earth is flat and non-rotating. Under this condition, the Earth-center Earth-fixed reference frame (ECEF) is equal to the Earth-fixed inertial reference frame.

2. The local horizon axes system $Ox_hy_hz_h$ is fixed to the airplane, with the origin O located at the center of gravity. Although it moves with the airplane, its axes remain parallel to the ground axes.

3. The wind axes system $Ox_wy_wz_w$ moves along with the airplane, with the x_w axis coincident with the velocity vector.

4. The body axes system $Ox_by_bz_b$ is fixed to the airplane itself. The X-axis of the body frame is pointed toward the aircraft nose, the Y-axis is along the right wing and Z-axis points down.

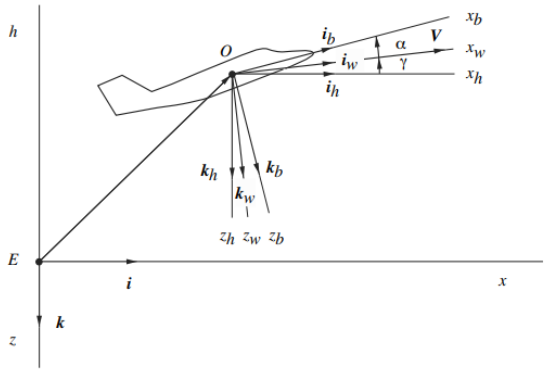

Figure 2.1: Coordinate Systems for Flight in a Vertical Plane ([7],p.18)

Observe the following relationships between the various frames:

- The body frame differs from the local horizon frame by the Euler angles ϕ, θ and ψ, which represent its orientation around the x, y, and z directions, respectively. (In the provided figure, θ corresponds to the sum of α and γ).
- The wind axes are offset from the local horizon axes by the flight path angle γ in the vertical direction and χ in the horizontal direction. This arrangement is made under the assumption that the atmosphere remains stationary relative to the ground ($V_w = 0$), and the aircraft's velocity relative to the air is equivalent to its velocity relative to the ground, aligning x_w with the aircraft velocity relative to the ground (V_k).
- The body axes align with the wind axes by the angle of attack α, the sideslip angle β and the bank angle μ. These angles describe the orientation of the aircraft relative to the oncoming airflow.

2.2 Rotation matrices

The equations of motion of the aircraft are derived for an axis system fixed to the airplane (body axes system). However, the position and orientation of the airplane cannot be described relative to the moving body axis frame and they have to be translated to a fixed frame of reference.To determine the orientation of the body frame in relation to the fixed frame, the following procedure can be employed:

Begin by envisioning the airplane positioned such that the body axis system aligns parallel to the fixed frame. Then, execute the following rotations:

1. Rotate the x-body, y-body, z-body frame around the Oz-axis by the yaw angle ψ, resulting in the frame being oriented as x1, y1, z1.

2. Rotate the x1, y1, z1 frame around the Oy-axis by the pitch angle θ, causing the frame to assume the configuration of x2, y2, z2.

3. Rotate the x2, y2, z2 frame around the Ox-axis by the roll angle ϕ, resulting in the frame aligning as x3, y3, z3. This represents the actual orientation of the body frame in relation to the fixed frame.

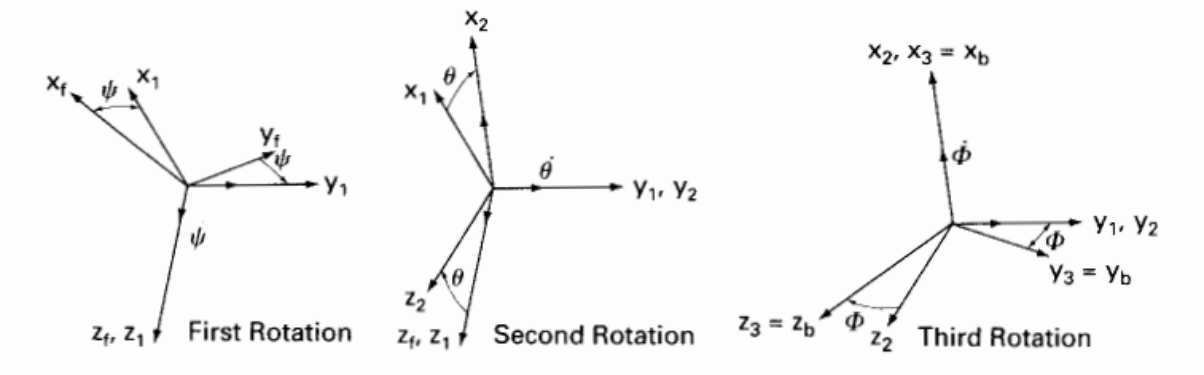

Figure 2.2: Relationship between body and inertial axes system ([10],p.102)

The transformation matrices, also known as Direction Cosine Matrices (DCMs), that achieve these three separate rotations are provided as follows :

- yaw rotation :

$$R(\psi) = \begin{pmatrix} \cos(\psi) & \sin(\psi) & 0 \\ -\sin(\psi) & \cos(\psi) & 0 \\ 0 & 0 & 1 \end{pmatrix} \tag{2.1}$$

- pitch rotation :

$$R(\theta) = \begin{pmatrix} \cos(\theta) & 0 & -\sin(\theta) \\ 0 & 1 & 0 \\ \sin(\theta) & 0 & \cos(\theta) \end{pmatrix} \tag{2.2}$$

- Roll rotation :

$$R(\phi) = \begin{pmatrix} 1 & 0 & 0 \\ 0 & \cos(\phi) & \sin(\phi) \\ 0 & -\sin(\phi) & \cos(\phi) \end{pmatrix} \tag{2.3}$$

In the field of aviation, it is common practice to describe an aircraft's attitude using the asymmetric choice of 3-2-1 Euler angles. Hence, to translate from the inertial frame to the body frame, the following expression is used:

$$\mathbf{r_B} = R(\phi)R(\theta)R(\psi)\mathbf{r_I} \tag{2.4}$$

To move the vector from the body frame to the inertial frame, we need to invert the rotations:

$$\begin{aligned} \mathbf{r_I} &= (R(\phi)R(\theta)R(\psi))^{-1}\mathbf{r_B} \\ &= R(\phi)^{-1}R(\theta)^{-1}R(\psi)^{-1}\mathbf{r_B} \\ &= R(-\psi)R(-\theta)R(-\phi)\mathbf{r_B} \end{aligned} \tag{2.5}$$

2.3 Mathematical modeling for MATLAB/Simulink

2.3.1 Calculation of forces and moments

Before beginning to model an aircraft, it is essential to take into account the forces and moments that act on it. In this regard, we will examine the commonly used sets of equations and formulations utilized for kinematics and dynamics modeling of a fixed-wing aircraft. A comprehensive guide is provided on this topic in [17]. Considering the aircraft model as a rigid body with six degrees of freedom (6 DOF), there are four distinct categories of forces and moments that impact the aircraft,namely:

- Gravitational force
- Aerodynamic forces
- Propulsion force
- Landing gear forces

1. Gravitational force

   The force of gravity on the aircraft can be illustrated by a vector aligned with the z-axis of the north-east-down frame that passes through the aircraft's center of gravity. To determine Earth's gravity at a particular location, we utilize the mathematical formula for the geocentric equipotential ellipsoid of the World Geodetic System (WGS84).

$$\tilde{\mathbf{F_G}} = \mathbf{m} \begin{bmatrix} 0 \\ 0 \\ g \end{bmatrix} \tag{2.6}$$

2. Aerodynamics forces

   The aerodynamic forces $\tilde{\mathbf{F_A}}$ and moments $\tilde{\mathbf{M_A}}$ can be computed as follows:

$$\tilde{\mathbf{F_A}} = QS \begin{bmatrix} -C_D \\ C_Q \\ -C_L \end{bmatrix} \tag{2.7}$$

$$\tilde{\mathbf{M_A}} = QS \begin{bmatrix} b.C_l \\ c.C_m \\ b.C_n \end{bmatrix} \tag{2.8}$$

   where Q is the dynamic pressure , given as $Q = \frac{1}{2}\rho V_a^2$, S is the wing surface area, b is the wingspan, c is the mean chord, C_D, C_Q and C_L are the drag, lateral force and

the lift coefficients respectively. Similarly, C_l, C_m and C_n are the roll moment, pitch moment and yaw moment coefficients respectively. The aerodynamic coefficients are given by the following formulas:

Aerodynamic force coefficients

- For the drag coefficient, a quadratic drag polar is used:

$$C_D = C_{D0} + k(C_l - C_{L0})^2 + C_{D\beta}\beta \tag{2.9}$$

- A linear relationship with alpha and the elevator deflection is employed to describe the lift coefficient:

$$C_L = C_{l0} + C_{L\alpha}\alpha + C_{L\eta}\eta \tag{2.10}$$

- The lateral force coefficient is influenced by the side slip angle and the rudder deflection:

$$C_Q = C_{Q\beta}\beta + C_{Q\zeta}\zeta \tag{2.11}$$

  where β is the side-slip angle, α is the angle of attack, η is the elevator deflection angle and ζ is the rudder deflection angle.

Aerodynamic moment coefficients

- The roll moment coefficient is given by :

$$C_l = C_{l\beta}\beta + C_{lp}p + C_{lr}r + C_{l\xi}\xi + C_{l\zeta}\zeta \tag{2.12}$$

- The pitch moment coefficient is given by :

$$C_m = C_{m\alpha}\alpha + C_{m\eta}\eta + C_{mq}q \tag{2.13}$$

- The yaw moment coefficient is given by:

$$C_n = C_{n\beta}\beta + C_{np}p + C_{nr}r + C_{n\xi}\xi + C_{n\zeta}\zeta \tag{2.14}$$

  where p, q, r represent the rotational rates and ξ the aileron angle of deflection.

3. Propulsion force

   In order to determine the propulsion force, we utilize the combined blade and element theory equation as outlined in [8]. This equation provides the rotor thrust based on the pitch angle and inflow ratio. It is important to note that the equation relies on the following assumptions:

   a) The propeller is ideally twisted with a constant chord

   b) The inflow is uniform

c) Interaction with the propeller vortex wake is not considered

d) The inflow ratio is positive, meaning there is no thrust reversal

Given these assumptions, we can determine the properties of the propeller as follows:

$$AR\,(aspect\,ratio) = \frac{2R}{C} \tag{2.15}$$

$$a = \frac{2\pi AR}{2 + AR} \tag{2.16}$$

$$\sigma = \frac{nC}{\pi R} \tag{2.17}$$

$$B(tiploss) = 1 - \frac{C}{2R} \tag{2.18}$$

where R is the propeller radius and C is the propeller chord and n is the number of propeller blades.

From here the induced velocity can be calculated as :

$$\lambda = \sqrt{(\frac{\sigma a}{16} - \frac{\lambda_c}{2})^2 + \frac{\sigma a}{8} * p} - (\frac{\sigma a}{16} - \frac{\lambda_c}{2}) \tag{2.19}$$

The variable p stands for the propeller pitch, while λ_c is the climb inflow ratio, which is calculated as $\frac{V_A}{\omega R}$. In this equation, V_A stands for airspeed, and ω represents the motor's angular velocity. To calculate the thrust coefficient, the following equation is used:

$$C_T = \frac{\sigma a}{4}(B)^2(p - \lambda) \tag{2.20}$$

Afterward, the thrust can be determined using this equation:

$$T = C_T \cdot \rho \cdot \pi \cdot R^2(R^2 \cdot \omega|\omega|) \tag{2.21}$$

4. Landing Gear forces

The landing gear of the aircraft can be modeled as a mass-spring-damper system :

The force acting on the landing gear (LG) can be divided into two components:

- A normal force acting perpendicular to the surface where the tire makes contact with the runway F_N
- A longitudinal force that acts parallel to the contact surface, typically given by the friction force, F_L

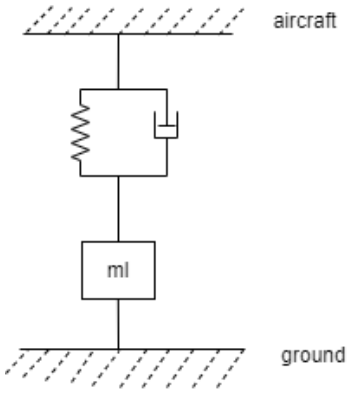

Figure 2.3: . The mass-spring-damper model used for the landing gear

a) Normal Force :

By analyzing the vertical equilibrium, one can determine the normal force exerted on the landing gear:

$$F_N = mg + m\ddot{z} + k(z - z_0) + c(\dot{z} - \dot{z_0}) \tag{2.22}$$

The variable z_0 represents the spring's fully relaxed position. It is important to note that $(z - z_0)$ cannot be negative due to a contact condition.

Consequently, the force acting on the aircraft itself due to the landing gear can be given by :

$$F_{Na} = F_N - mg = m\ddot{z} + k(z - z_0) + c(\dot{z} - \dot{z_0}) \tag{2.23}$$

b) Longitudinal Force :

The initial step involves determining whether the aircraft has landed or not. To achieve this, we begin by considering the initial compressed spring length denoted as h_0. Additionally, we calculate the compression length of the spring-damper system when the aircraft is resting on the ground, taking into account the aircraft mass (m) and the virtual rod stiffness (c). This calculation is expressed as:

$$dl_0 = \frac{mg}{c} \tag{2.24}$$

Thus, the total undeformed length of the spring is given by $h_0 + dl_0$.

Next, we proceed to check if the aircraft is in contact with the ground, considering the actual height (h) of the aircraft's center of gravity above the ground

level, as well as the values of h_0 and dl_0. If the condition $h > h_0 + dl_0$ is met, it indicates that the aircraft is not touching the ground. Consequently, no forces and moments act on the aircraft from the ground.[5]

On the other hand, if ground contact is detected, we can determine the longitudinal force, which primarily represents the braking force in the aircraft's longitudinal direction. Additionally, there will be a lateral force compensating for all the other forces acting on the aircraft, including the gravitational force, propulsive force, aerodynamic forces, and the landing gear's normal force.

Finally, we can compute the braking force as:

$$F_b = \mu_L . F_N \tag{2.25}$$

where μ_L is the longitudinal friction coefficient.

2.4 Aircraft equations of motion

Assume that the position of the aircraft in the inertial frame is given by the vector $x = [x, y, z]^T$ where x, y and z denote the position of the aircraft in the North, East and down directions, respectively. The motion of the aircraft is clearly defined by the kinematic and dynamic relations for the translational and rotational directions, which can be looked up in [9] and [15].

Translational Kinematics

$$\dot{x_\Delta} = \begin{pmatrix} \dot{y_\Delta} \\ \dot{z_\Delta} \end{pmatrix} = V_k \begin{pmatrix} \cos(\gamma)\sin(\chi - \chi_0) \\ \cos(\gamma)\sin(\gamma_0)\cos(\chi - \chi_0) - \sin(\gamma)\cos(\gamma_0) \end{pmatrix} \tag{2.26}$$

Where γ_0 and χ_0 represent the inclination and azimuth angles of the desired reference path.

Translational Dynamics

$$\dot{v} = \begin{pmatrix} \dot{V_a} \\ \dot{\gamma} \\ \dot{\chi} \end{pmatrix} = \frac{1}{V_a m} \begin{pmatrix} -V_a(D(\alpha, V_a) - \cos(\alpha + i_T)T(\delta_F)) - V_a mg\sin(\gamma) \\ \cos(\mu)(L(\alpha, V_a) + \sin(\alpha + i_T)T(\delta_F) - mg\cos(\gamma) \\ \sin(\mu)(L(\alpha, V_a) + \sin(\alpha + i_T)T(\delta - F))\frac{1}{\cos(\gamma)} \end{pmatrix} \tag{2.27}$$

Rotational Kinematics

$$\dot{\phi} = \begin{pmatrix} \dot{\mu} \\ \dot{\alpha} \\ \dot{\beta} \end{pmatrix} = \begin{pmatrix} \cos(\alpha)cos(\beta) & 0 & sin(\alpha) \\ \sin(\beta) & 1 & 0 \\ \sin(\alpha)cos(\beta) & 0 & -cos(\alpha) \end{pmatrix}^{-1} \left(\omega - T_{fk} \begin{pmatrix} -\dot{\chi}\sin(\gamma) \\ \dot{\gamma} \\ \dot{\chi}\cos(\gamma) \end{pmatrix} \right) \tag{2.28}$$

where $T_{fk} = \begin{pmatrix} \cos(\alpha)\cos(\beta) & -\cos(\alpha)\sin(\beta)\cos(\mu)+\sin(\alpha)\sin(\mu) & -\cos(\alpha)\sin(\beta)\sin(\mu)-\sin(\alpha)\cos(\mu) \\ \sin(\beta) & \cos(\beta)\cos(\mu) & \cos(\beta)\sin(\mu) \\ \sin(\alpha)\cos(\beta) & -\sin(\alpha)\sin(\beta)\cos(\mu)-\cos(\alpha)\sin(\mu) & -\sin(\alpha)\sin(\beta)\sin(\mu)+\cos(\alpha)\cos(\mu) \end{pmatrix}$ represents a transformation from the path to the body frame and ω is the angular rates vector.

Rotational Dynamics

$$\begin{aligned} \dot{\omega} &= \begin{pmatrix} \dot{p} \\ \dot{q} \\ \dot{r} \end{pmatrix} = \mathbf{J^{-1}}(\mathbf{M}(\omega, \delta) - \omega \times \mathbf{J}\omega) \\ &= \frac{1}{I_{xx}I_{ZZ} - I_{xz}^2} \begin{pmatrix} I_{zz} & 0 & -I_{xz} \\ 0 & \frac{1}{I_{yy}} & 0 \\ -I_{xz} & 0 & I_{xx} \end{pmatrix} \left[\begin{pmatrix} L \\ M \\ N \end{pmatrix} - \begin{pmatrix} p \\ q \\ r \end{pmatrix} \mathbf{x} \begin{pmatrix} I_{xx} & 0 & I_{xz} \\ 0 & I_{yy} & 0 \\ I_{xz} & 0 & I_{zz} \end{pmatrix} \begin{pmatrix} p \\ q \\ r \end{pmatrix} \right] \end{aligned} \tag{2.29}$$

2.5 Control Techniques

Prior to the 1990s, classical, linear control techniques were the primary approach used in flight control systems for fixed-wing aircraft [4]. Although these methods produced satisfactory outcomes under nominal conditions, it is well-known that their validity is limited to small-range operation. As the required operational range expands, the performance of linear control methods deteriorates, leading to potential instability, mainly due to their inadequate compensation for the system's inherent non-linearities [13].Thus, to account for the non-linear characteristics of aircraft dynamics, it was necessary to utilize various control gains tailored for different operating points. Commonly, gain scheduling was used to accomplish this task. However, implementing gain scheduling was time-consuming, expensive, and heavily dependent on engineering expertise [6].

To overcome these limitations, advanced control techniques such as model predictive control (MPC), adaptive control, or nonlinear control methods are being explored for UAV applications. One widely used multivariable control technique is Nonlinear Dynamic Inversion (NDI), which avoids gain-scheduling and directly incorporates nonlinearities into the control laws. [6].This leads to reduced development costs and time, easier reuse across various airframes, greater ability to

cope with changing models, and improved performance at high angles of attack compared to classical control techniques[16]. However, NDI has a drawback in that model mismatches and measurement errors can reduce performance and even result in unstable situations.[12].

To address these issues, Incremental Nonlinear Dynamic Inversion (INDI) was developed. INDI retains the benefits of NDI while increasing controller robustness to model uncertainties and decreasing the controller's dependence on the vehicle model[12]. In the following sections, the mathematical derivation of NDI and INDI is provided, and the reduced dependency on an exact mathematical model of the system to be controlled is illustrated.

2.5.1 Non-linear dynamic inversion

Non-linear Dynamic Inversion (NDI), also referred to as exact linearization, provides a systematic approach to cancel the system dynamics and subsequently control the system as a linear system. This is done by finding a direct relation between the desired output and the input and inverting it to get the control law. For the purpose of clarification, an example provided in [12] is discussed here. Consider a general first-order linear system :

$$\dot{x} = f(x) + \bar{G}(x)u \tag{2.30}$$

$$y = h(x) \tag{2.31}$$

where $\mathbf{x}$ is the state vector, $\mathbf{u}$ is the input vector and $\mathbf{y}$ is the output vector.

By differentiating equation 2.31:

$$\begin{aligned} \dot{y} = \frac{dh(x)}{dt} &= \frac{\partial h(x)}{\partial x}.\frac{dx}{dt} \\ &= \nabla h(x)\dot{x} = \nabla h(x)[f(x) + \bar{G}(x)u] \\ &= \nabla h(x)f(x) + h(x)\bar{G}(x)u \\ &= L_f h(x) + L_g h(x)u \end{aligned} \tag{2.32}$$

Thus, a relation between the input and output can be given by :

$$\dot{y} = L_f h(x) + L_g h(x)u \tag{2.33}$$

To find the control law, replace $\dot{y}$ by v:

$$u = L_g h(x)^{-1}(v - L_f h(x)) \tag{2.34}$$

where the pseudo-control input, denoted by v, is a signal tracked by the derivative of the output. Consequently, the output can be controlled by selecting an appropriate value for v.

Extending this notion to a more particular concept, consider the aircraft's angular rates which can be expressed using the following equation:

$$J\dot{\omega} + \omega \times J\omega = M = M_a + M_c \tag{2.35}$$

Note that the moment M is a combination of two components: M_a generated by the aerodynamics of the airframe, and M_c generated by the deflection of the control surfaces. The latter is described by the control derivatives multiplied by the deflection angle δ. As a result, the equation can be written as follows:

$$J\dot{\omega} + \omega \times J\omega = M_a + (M_c)_\delta \delta \tag{2.36}$$

Solving equation 2.35 for $\dot{\omega}$:

$$\dot{\omega} = J^{-1}(M_a + M_c - \omega \times J\omega) \tag{2.37}$$

By applying NDI to this equation and considering that $M_c = (M_c)_\delta \delta$, we can derive an expression for the aircraft's input δ. :

$$\delta = (M_c)_\delta^{-1}(Jv + \omega \times J\omega - M_a) \tag{2.38}$$

The fundamental premise of this control law relies on the accurate definition of the entire aerodynamic model encapsulated in M_a and M_c. As a result, the control law's effectiveness will be influenced by any uncertainties present in the aerodynamic model.

2.5.2 Incremental Non-linear dynamic inversion

Rather than calculating the total deflection of the control surfaces during each execution, it is possible to compute only the increments of the respective control surface deflections. To accomplish this, we need to rewrite the rotational dynamic equation of motion in an incremental form, which can be achieved through the utilization of a Taylor series expansion.

$$\begin{aligned}\dot{\omega} = {} & J^{-1}(M_{a0} - \omega_0 \times J\omega_0 + M_{c0}) \\ & + \frac{\partial}{\partial \omega}[J^{-1}(M_a - \omega \times J\omega + M_{c]})]_{\omega=\omega_0, \delta=\delta_0}(\omega - \omega_0) \\ & + \frac{\partial}{\partial \delta}[J^{-1}(M_a - \omega \times J\omega + M_c)]_{\omega=\omega_0, \delta=\delta_0}(\delta - \delta_0)\end{aligned} \tag{2.39}$$

Noting that the term $\mathbf{J^{-1}}(\mathbf{M_{a0}} - \omega_\mathbf{0} \times \mathbf{J}\omega_\mathbf{0} + \mathbf{M_{c0}})$ is nothing but $\dot{\omega_\mathbf{0}}$ and by eliminating the parts of the equation that are independent of the angular rates and/or the control surface deflection, equation 2.39 can be simplified into the following:

$$\dot{\omega} \approx \dot{\omega_0} + \frac{\partial}{\partial \omega}[J^{-1}(M_a - \omega \times J\omega)]_{\omega=\omega_0,\delta=\delta_0}(\omega - \omega_0) + \frac{\partial}{\partial \delta}[J^{-1}M_c]_{\omega=\omega_0,\delta=\delta_0}(\delta - \delta_0) \quad (2.40)$$

Equation 2.40 can be further simplified, given that, for incremental time advances, the second term on the right-hand side is significantly smaller than the third term. The reason behind this lies in the following explanation: When there is a change in the aircraft's control input, it results in a corresponding change in the moment exerted on the aircraft. This moment, in turn, directly affects the aircraft's angular accelerations, which describe how its angular rates change over time. On the other hand, the angular rates change primarily through the integration of angular accelerations, which includes the contribution from control surface deflection. For small time increments, the change in angular rates caused directly by control surface deflection is so negligible that it can be disregarded. This assumption holds under the consideration that the demanded deflection of the control surface is achieved instantaneously, without any significant time delay:

$$\dot{\omega} = \dot{\omega_0} + \frac{\partial}{\partial \delta}[J^{-1}M_c]_{\omega=\omega_0,\delta=\delta_0}(\delta - \delta_0) \quad (2.41)$$

Assuming a linear relation between control deflection and control moment,the last equation can finally be rewritten into :

$$\dot{\omega} = \dot{\omega_0} + J^{-1}(M_c)_\delta d\delta \quad (2.42)$$

The updated version of the dynamic rotational equation of motion has three significant implications. Firstly, the aerodynamic moment term, M_a, is no longer present in the equation. This implies that the angular acceleration is no longer expressed in terms of the largest part of the aerodynamic model. Secondly, the M_a term was dependent on the center of gravity's location through the definition of the aerodynamic model, which is now eliminated as well. Finally, the expression no longer contains the nonlinear cross-couplings of angular rates, $\omega \times \mathbf{J}\omega$.

Using the newly found equation, we apply NDI, where the output is defined as $y = \omega$:

$$\dot{y} = \dot{\omega} = \omega_0 + J^{-1}(M_c)_\delta d\delta \quad (2.43)$$

Replacing the angular acceleration with the pseudo-control input $\dot{\omega} = v$;

$$d\delta = (M_c)_\delta^{-1} J(v - \dot{\omega_0}) \tag{2.44}$$

To calculate the full control surface deflection :

$$u = \delta = \delta_0 + d\delta \tag{2.45}$$

It can be deduced that when applying Nonlinear Dynamic Inversion (NDI) to the incremental form of the equation, the resulting control law becomes independent of the largest part of the aerodynamic model, given by M_a, thereby avoiding the influence of significant aerodynamic uncertainties. Unlike conventional Nonlinear Dynamic Inversion (NDI) methods that require precise knowledge of the system for explicit cancellation, the approach described here doesn't depend on achieving such high accuracy, which is often impractical and challenging in real-world scenarios.

INDI can, thus, be defined as a combined model– and sensor-based control approach. It operates effectively with only a control effectiveness model and measurements of the state and some of its derivatives, as will become more evident in subsection3.2.1. As a result, it significantly reduces its reliance on precise knowledge of the complete system dynamics.[2]

3 Methodology

The workflow suggested for this research is presented in Figure 3.1. It begins with the selection of an appropriate airfoil and the identification of necessary measurements. These measurements are then used to construct a model in XFLR5, an open-source software package that models the airfoil and allows for aerodynamic and stability/control analysis based on 3D panel method, VLM, and Lifting Line Theory. The next step involves developing a UAV system architecture model and conducting simulations using MATLAB/SIMULINK to test the model's capabilities. Finally, flight tests are proposed as the last stage of the process.

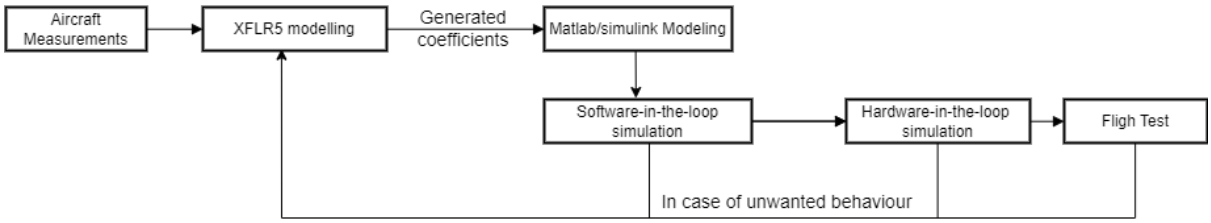

Figure 3.1: Proposed Workflow

3.1 XFLR5 analysis

3.1.1 Airframe measurement

Figure 3.2: Multiplex FunCub XL ND

The plane used for this research is the FUNCUB XL ND made by Multiplex. It is a versatile high-wing aerobatic aircraft designed for RC model flying. The plane was altered to include an on-board computer, sensors, batteries, and other necessary equipment. The manufacturer has provided the following technical specifications:

Wingspan	1700 mm
Material	Elapor
Recommended battery	65 LiPo
Take-Off weight Electric	2650 g
Elevator	yes
Rudder	yes
Aileron	yes
Flaps	yes

3.1.2 Main wing

The main wing consists of two half-wings that are geometrically symmetric and meet at the fuselage's midpoint. Therefore, the information provided pertains to

one half-wing, but it can be extrapolated to the other half. The weight of the right wing was measured using a digital scale and found to be 0.368 kg. The span of the wing was measured to be 0.78 m, with a root chord of 0.260 m that decreases uniformly to reach 0.100 m at the tip of the wing. Additionally, a flap is present, starting from the wing root and extending to a distance of 0.295 m from the centerline (wing root). The aileron, on the other hand, begins at 0.295 m and extends to 0.675 m from the wing root. Measurements were taken for both the aileron and flap deflections. The flap is capable of deflecting nearly 90 degrees in the downward direction (+90 degrees, with the positive sign indicating the trailing edge downward). On the other hand, the aileron can deflect up to 50 degrees in both directions (+50 degrees and -50 degrees). With a vernier caliper and markers, a maximum camber of 1.8% of the chord length at the 21% interval along the chord line was measured. The maximum thickness of the wing section was measured to be 12% and at around 12.28% of the chord length. By standard NACA 4-digit airfoil designation convention, this identifies it as a NACA 2212 airfoil that is modified to fit the measurements given.

In summary, the given data is presented in the following table:

Table 3.1: Wing Measurement Data

Parameter	Value
Weight of the wing	0.368 kg
Wing span	0.78 m
Root chord	0.260 m
Tip chord	0.100 m
Flap start	0.000 m
Flap end	0.295 m
Aileron start	0.295 m
Aileron end	0.675 m
Flap deflection	+90 degrees
Aileron deflection	+50 degrees, -50 degrees
Maximum camber	1.8% at 21% chord
Maximum thickness	12% at 12.28% chord
Airfoil type	NACA 2212 (modified)

3.1.3 Elevator and fin

The elevator was weighed and recorded to have a weight of 0.070 kg, with a chord length of 0.240 m and a span of 0.285 m. Meanwhile, the fin has a weight of 0.035

kg, a chord length of 0.285 m, and a span of 0.300 m. The airfoil used for both of them is the standard airfoil NACA 0010.

Table 3.2: Elevator & Fin Measurement Data

Component	Weight (kg)	Chord Length (m)	Span (m)
Elevator	0.070	0.240	0.285
Fin	0.035	0.285	0.300
Airfoil	NACA 0010 (standard)		

3.1.4 XFLR5 model

XFLR5 is a tool that analyzes airfoils, wings, and planes that operate at low Reynolds Numbers. It can use the XFOIL code for airfoil analysis and can also predict stability and control derivatives, which are crucial for modeling. To create an aircraft model, the following steps are taken:

a) Airfoil Creation:

To investigate the aerodynamic behavior of our model in XFLR5, the aerofoils had to be identified as previously shown and modeled. The two primary foils were the NACA 2212 (main wing), NACA 0010 (for the horizontal and vertical stabilizers). To accurately model the representative foils on the sections of the modeled surfaces where different control surfaces are present, modifications were made to the primary foils. All the airfoils were generated with an initial assignment of 150 panels and Global Refinement was used to ensure panel distribution prior to analysis.

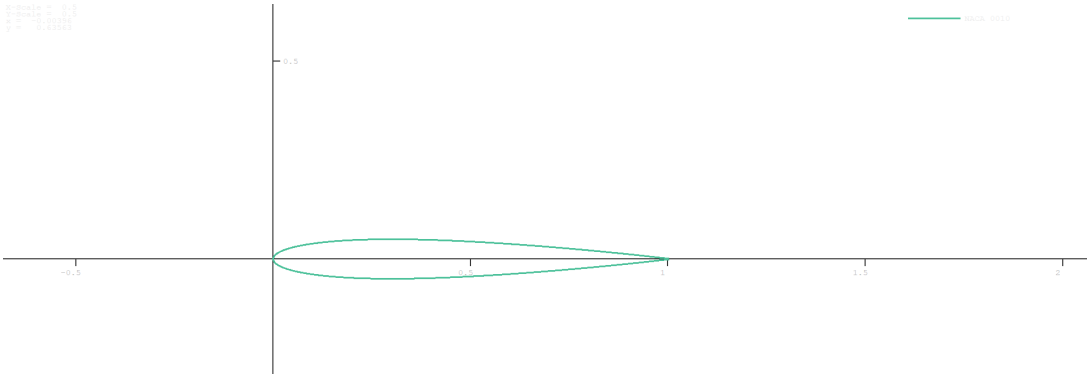

(a) NACA 0010

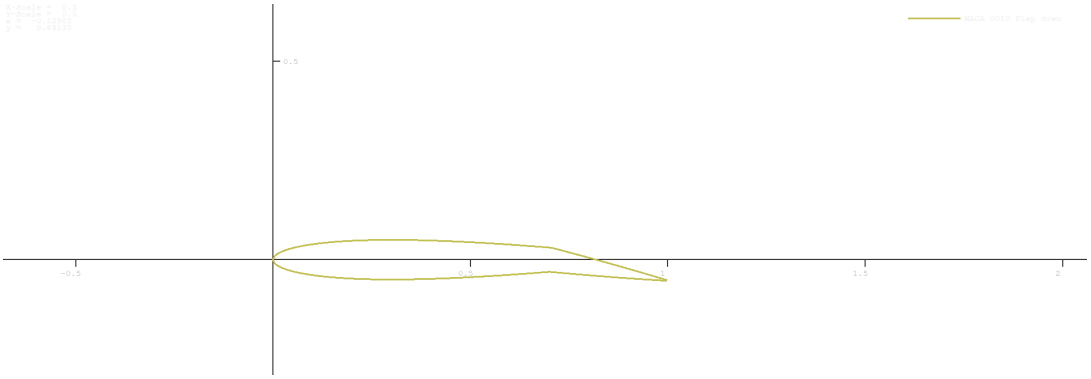

(b) NACA 0010 down

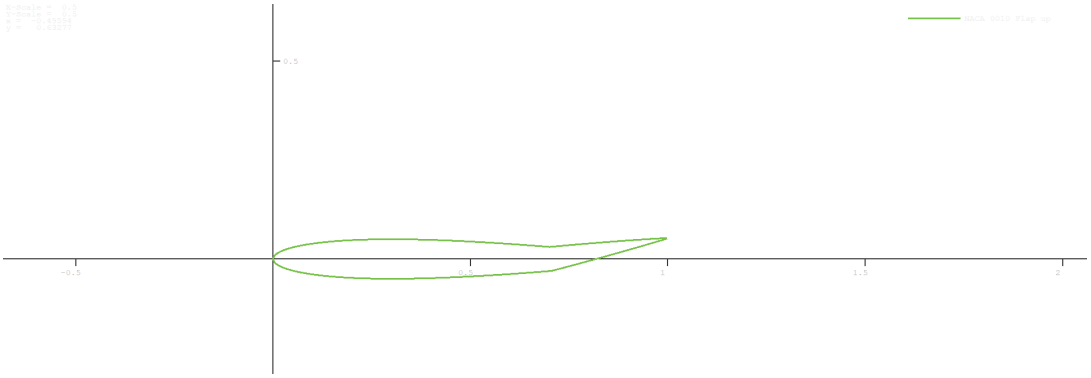

(c) NACA 0010 up

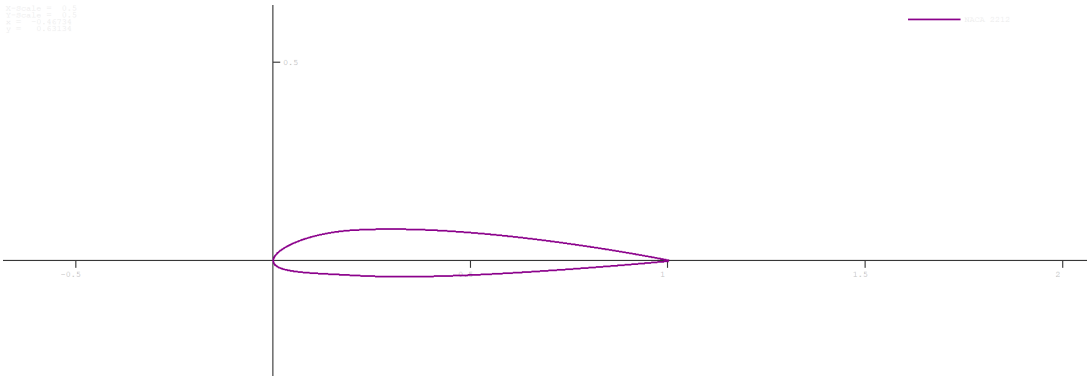

(a) NACA 2212

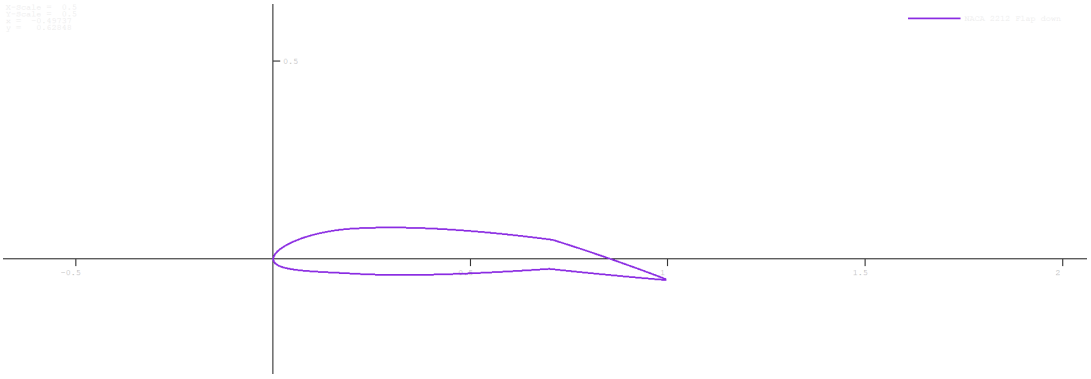

(b) NACA 2212 down

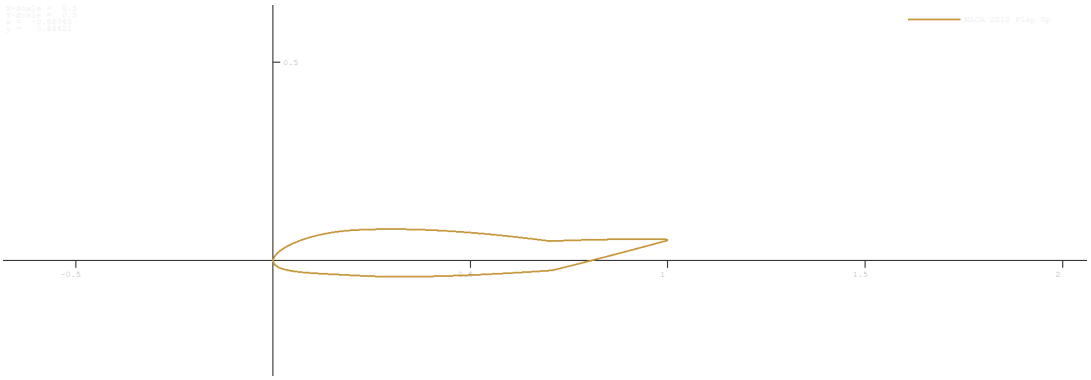

(c) NACA 2212 up

Figure 3.4: Airfoils used in the analysis.

b) Airfoil Analysis :

To gather all the necessary aerodynamic data on the identified airfoils and their variants, a 2D analysis was conducted on these airfoils. Initially, a batch analysis was performed for a range of Reynolds numbers from 10,000 to 500,000, with alpha varying from -20 to 20 in 0.5-degree increments. However, it was experimentally discovered that certain sections of the airfoils can have a local Reynolds number that is above/below that range. Consequently, distinct sets of polars were generated to patch those regions and ensure a higher level of simulation fidelity. This dataset facilitates additional analysis of 3D sections and complete models, enhancing the overall understanding and evaluation of the aerodynamic characteristics

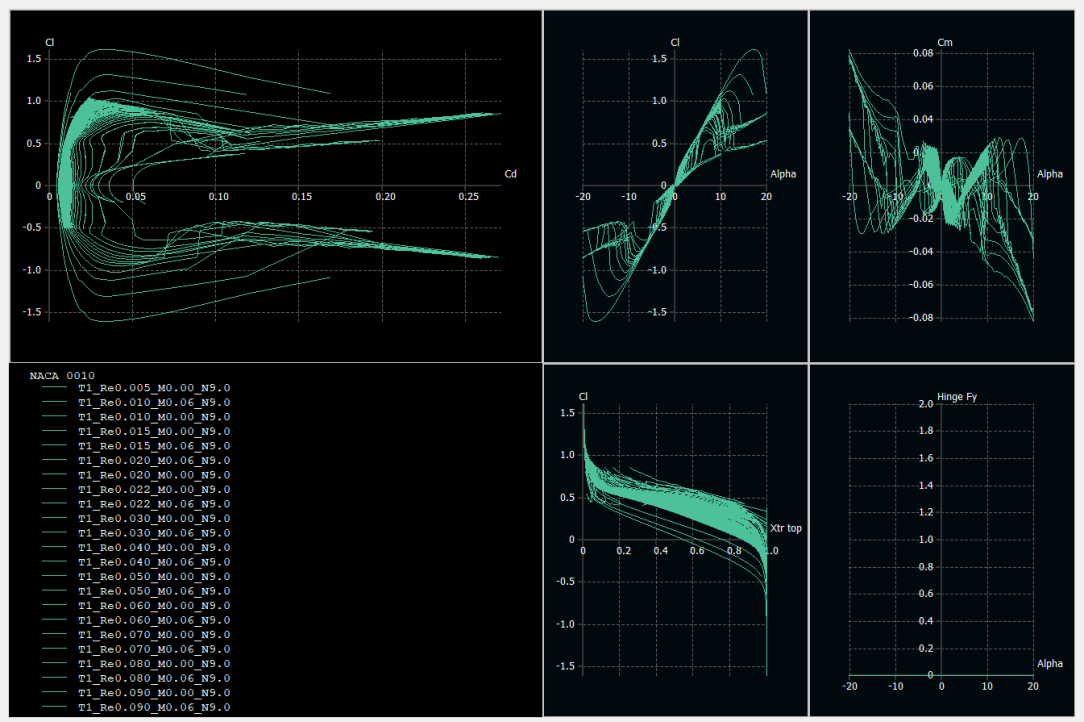

Figure 3.5: NACA 0010 analysis

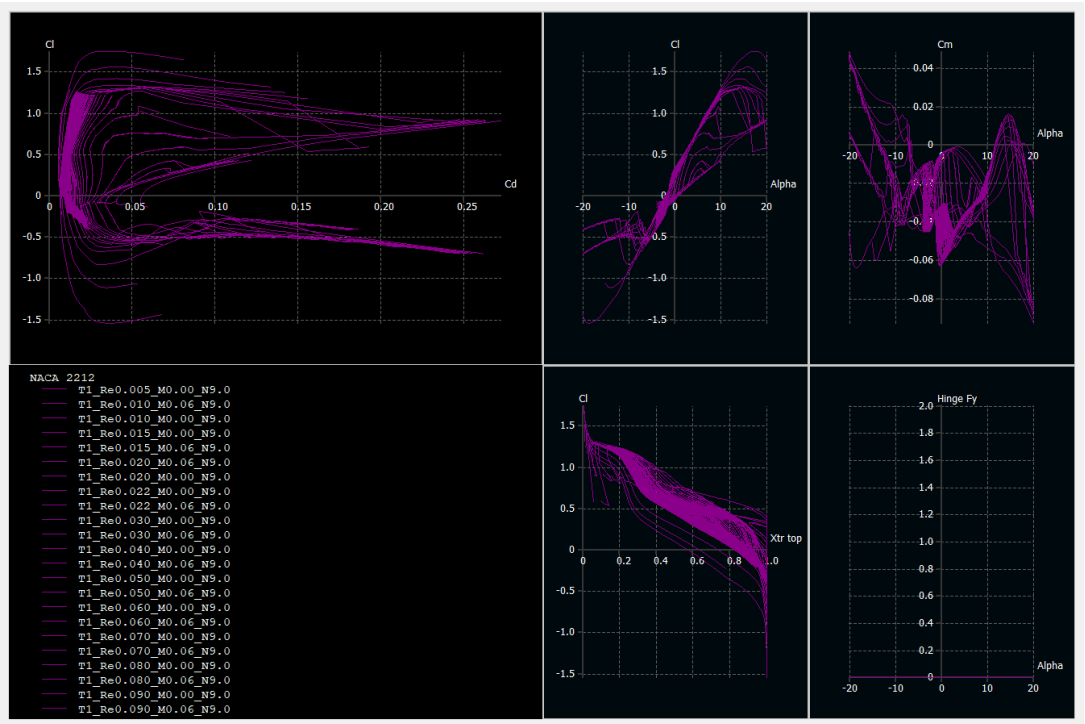

Figure 3.6: NACA 2212 analysis

c) Plane Modelling :

After generating the airfoils and conducting a 2D viscous analysis on them, a 3D model of the plane was created. The fuselage geometry was not included in the model as a 3D surface due to numerical issues that arise when using XFLR5's analytical methods with a fuselage. Therefore, the 3D representation of the fuselage was omitted during the modeling process. However, in order to enhance the accuracy of the dynamic modeling, other components were modeled as point masses, including the fuselage, based on prior measurements. After that, the following analyses were run on the 3d model :

- Performance analysis : Type one(fixed speed) analysis is run for velocities 5,10,14,18,22,26,30,40 each for alpha ranging from -10 to 10 with increments of 1. This is repeated for Betas 5,10 and 15
- Stability Analysis: In this section, stability parameters were obtained through static and dynamic tests. These parameters are valuable in assessing the stability of the system. An analysis of Type 7 (T7-VLM2) was conducted by adjusting one control parameter at a time, with the gain set to one for each parameter individually.

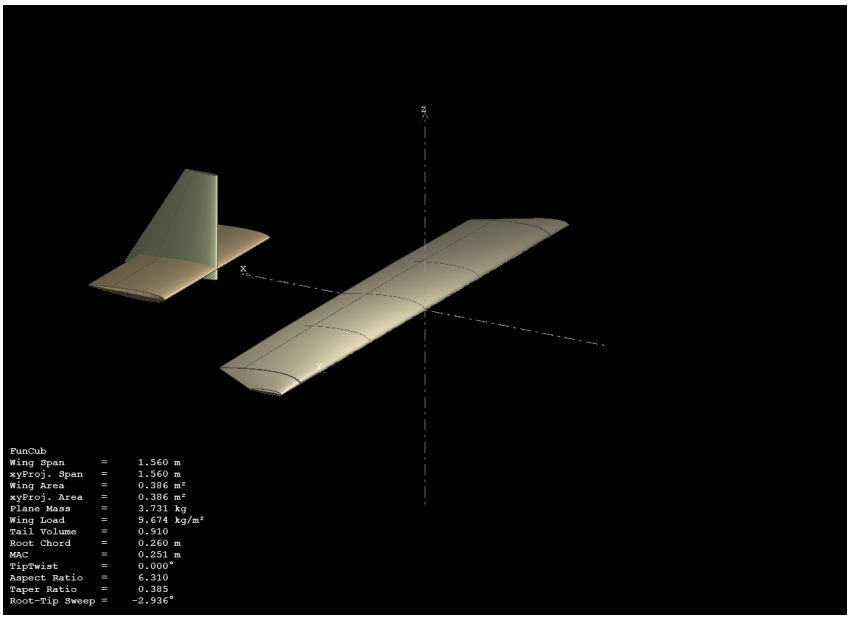

Figure 3.7: 3D model of the plane

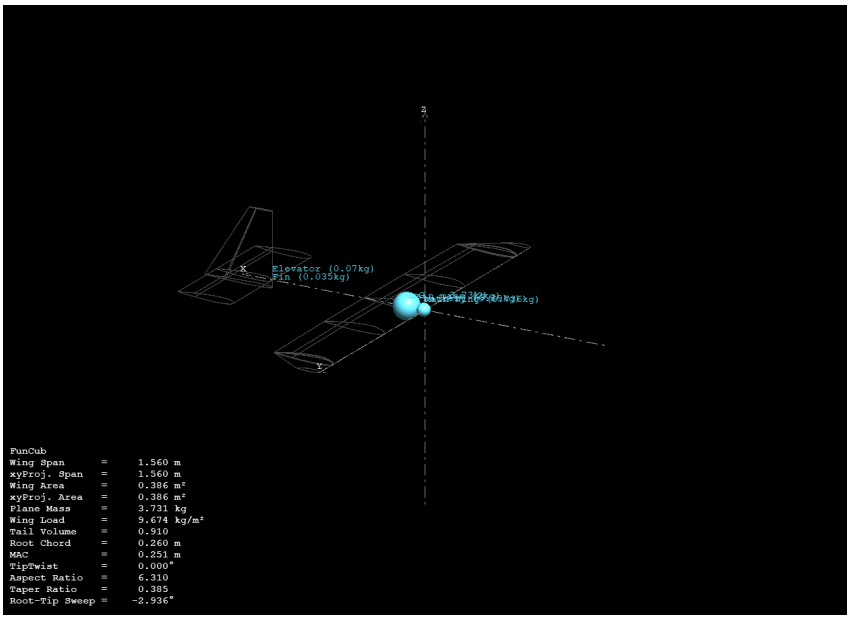

Figure 3.8: Masses & CoG representation

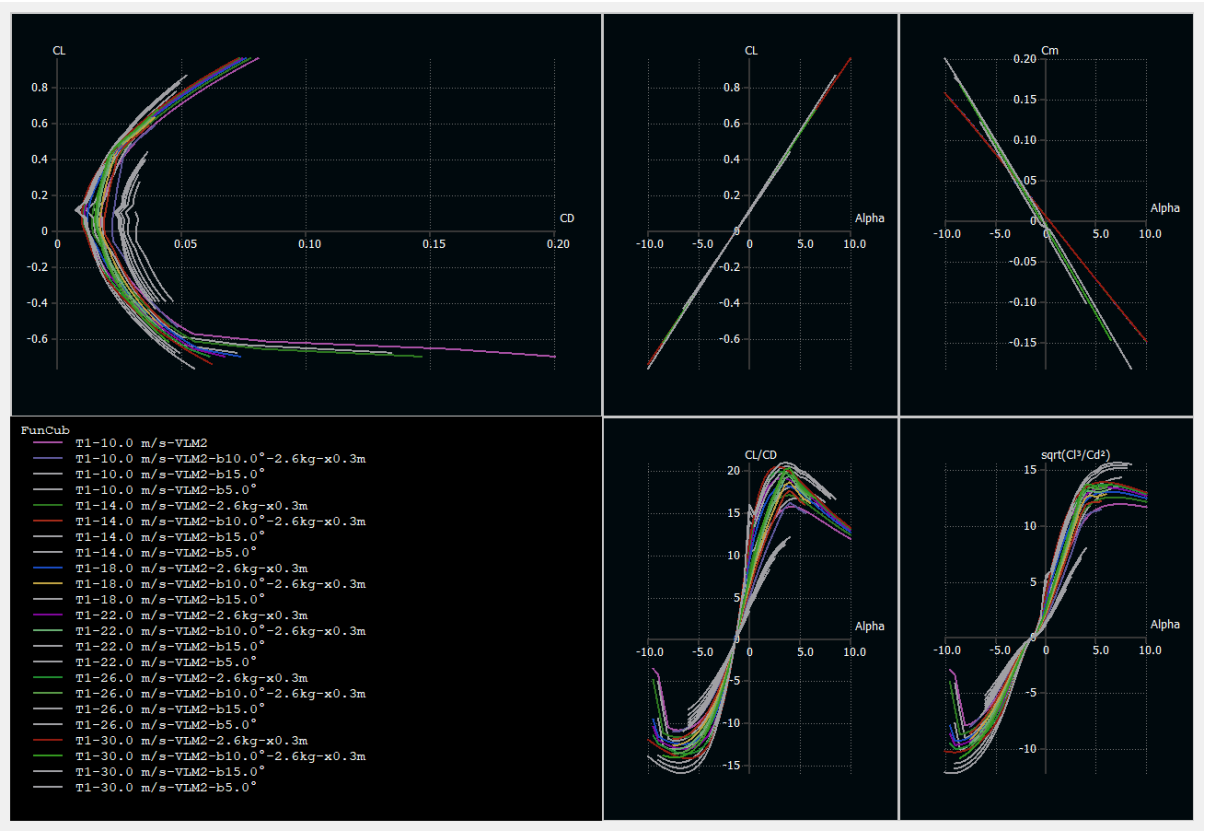

Figure 3.9: Analysis results

The two key observations here are:

Firstly, the negative slope of the curves $C_m = \mathrm{f}(\alpha)$ indicates static stability. This means that the aircraft exhibits a tendency to return to its original equilibrium position after experiencing disturbances. Such stability is crucial for safe and controlled flight. Secondly, the fact that the lift coefficient remains positive for each angle of attack (AOA) leading to $C_m = 0$ implies that the plane is capable of sustained flight. This is because the lift generated by the wings balances the aircraft's weight, enabling it to remain airborne. These two aspects contribute to the overall stability and flight performance of the aircraft.

3.2 Simulink Model

With MATLAB and Simulink, the flight control algorithm is designed and simulated with a UAV plant model that represents the aircraft under study while including environmental factors.

The control structure comprises four loops, namely the position control, velocity control, attitude control, and angular rate control, which are arranged in a cascaded structure. In essence, each control loop establishes the set points for the subsequent one. The cascaded design enables the use of various control methods tailored to the unique characteristics of each control variable. This ensures that the requirements of the different phases of ATOL are met and that quantity limitations are applied between control loops.. The NDI control approach is used to design the position and attitude control loops, since the kinematics equations, both rotational and translational (2.28 & 2.26), do not have any coefficients that rely on the specific model. On the other hand, the INDI control approach is used for the flight path and angular rate control loops due to the presence of model uncertainties. More details about these four loops are given in the following :

a) Position control loop: The aim is to track the trajectory reference accurately. This loop generates the desired references for χ_{cmd} and γ_{cmd}.

b) Velocity control loop: It aims to steer the aircraft towards the reference values of $[V, \chi, \gamma]_{ref}$ given in the first loop. It generates the necessary commands, such as α_{cmd} and μ_{cmd}, for the attitude control loop. Moreover, it generates the required thrust command to follow the velocity reference V.

c) Attitude control loop: The objective is to follow the reference values given by the velocity control loop and to generate the desired angular rates $[p, q, r]_{cmd}$, which will be fed to the angular rate loop.

d) Angular rate control loop: It is responsible for tracking the desired rates set by the attitude control loop. Its main purpose is to send the necessary command to the actuators in order to achieve the desired objective.

3.2.1 Derivation

The following section illustrates the control law derivation of each loop as given in [14] and [11] .

a) **Rate control**:

The desired rotation rates $\omega = \begin{pmatrix} p & q & r \end{pmatrix}^T$ are translated into corresponding control surface deflections. $\delta = \begin{pmatrix} \xi & \eta & \zeta \end{pmatrix}^T$

As given by equation 2.42:

$$\dot{\omega} = \dot{\omega_0} + J^{-1}(M_c)_\delta d\delta \tag{3.1}$$

and since

$$(M_c)_\delta = \frac{1}{2}\rho V^2 S \begin{bmatrix} C_{L\delta a} & 0 & C_{L\delta r} \\ 0 & C_{m\delta e} & 0 \\ C_{n\delta a} & 0 & C_{n\delta r} \end{bmatrix} \begin{pmatrix} b \\ c \\ b \end{pmatrix} \tag{3.2}$$

Therefore:

$$\dot{\omega} = \dot{\omega_0} + qS \begin{pmatrix} \frac{-bI_{zz}}{I_{xz}{}^2 - I_{xx}I_{zz}} & 0 & \frac{bI_{xz}}{I_{xz}{}^2 - I_{xx}I_{zz}} \\ 0 & \frac{c}{I_{yy}} & 0 \\ \frac{bI_{xz}}{I_{xz}{}^2 - I_{xx}I_{zz}} & 0 & \frac{-bI_{xx}}{I_{xz}{}^2 - I_{xx}I_{zz}} \end{pmatrix} \begin{bmatrix} \frac{\partial C_L}{\partial \xi} & 0 & \frac{\partial C_L}{\partial \zeta} \\ 0 & \frac{\partial C_m}{\partial \eta} & 0 \\ \frac{\partial C_n}{\partial \zeta} & 0 & \frac{\partial C_n}{\partial \zeta} \end{bmatrix} \Delta\delta \tag{3.3}$$

For simplicity the term

$$qS \begin{pmatrix} \frac{-bI_{zz}}{I_{xz}{}^2 - I_{xx}I_{zz}} & 0 & \frac{bI_{xz}}{I_{xz}{}^2 - I_{xx}I_{zz}} \\ 0 & \frac{c}{I_{yy}} & 0 \\ \frac{bI_{xz}}{I_{xz}{}^2 - I_{xx}I_{zz}} & 0 & \frac{-bI_{xx}}{I_{xz}{}^2 - I_{xx}I_{zz}} \end{pmatrix} \begin{bmatrix} \frac{\partial C_L}{\partial \xi} & 0 & \frac{\partial C_L}{\partial \zeta} \\ 0 & \frac{\partial C_m}{\partial \eta} & 0 \\ \frac{\partial C_n}{\partial \zeta} & 0 & \frac{\partial C_n}{\partial \zeta} \end{bmatrix} \longrightarrow B_\omega$$

Thus, equation 3.3 can be rewritten as :

$$\dot{\omega} = \dot{\omega_0} + B_\omega \Delta\delta \tag{3.4}$$

To convert this system into a linear system, we substitute $\dot{\omega}$ with v_ω. This is a pseudo-control given by the first order system $K_\omega(\omega_c - \omega_m)$, where K_ω is a diagonal matrix with values K_p, K_q, and K_r.

As a result :

$$K_\omega(\omega_c - \omega_m) = \dot{\omega_0} + B_\omega \Delta\delta \tag{3.5}$$

In order to determine the real control variable, which is represented by $\Delta\delta$, we solve for it and replace the state $\dot{\omega_0}$ at the local linearization point by the estimated angular acceleration $\dot{\omega_a}$ at every time step:

$$\Delta\delta = B_\omega^{-1}(K_\omega(\omega_c - \omega_m) - \dot{\omega_a}) \tag{3.6}$$

To obtain the total control law, the incremental command is simply added to the current deflections.

b) **Attitude control**:

In order to control the attitude, this loop converts the commanded angles, $\phi = (\mu, \alpha, \beta)^T$, into their corresponding angular rates, $\omega = (p, q, r)^T$. There is no need to use INDI in this scenario, as previously explained, so conventional NDI is applied to the rotational kinematics equation 2.28 and the right-hand side of the equation $\dot{\phi}$ is replaced by the pseudo-control variable $V_\alpha = K_\alpha(\alpha_c - \alpha_m)$ with $K_\alpha = diag\{K_\mu, K_\alpha, K_\beta\}$.

Solving for the control variable in this loop, namely, ω :

$$\omega = \begin{pmatrix} p \\ q \\ r \end{pmatrix} = T_\alpha K_\alpha(\alpha_c - \alpha_m) + T_{fk} \begin{pmatrix} -\dot{\chi}\sin(\gamma) \\ \dot{\gamma} \\ \dot{\chi}\cos(\gamma) \end{pmatrix} \tag{3.7}$$

c) **Velocity control**:

This process converts the instructed velocity vector $\mathbf{v} = (V_a, \gamma, \chi)$ into the relevant aerodynamic angles μ and α and the thrust δ_f. Linearizing the translational dynamics equation 2.27 with a first-order Taylor expansion results in :

$$\dot{\mathbf{v}} = \dot{\mathbf{v}}_\mathbf{0} + B_v \begin{pmatrix} \Delta\delta \\ \Delta\alpha \\ \Delta\mu \end{pmatrix} \tag{3.8}$$

where, as given in [14], B_v can be approximated by:

$$B_v \approx \frac{1}{V_a m} \begin{pmatrix} V_a T_\delta \cos(\alpha) & V_a C_{D\alpha} qS & 0 \\ T_\delta \cos(\mu)\sin(\alpha) & C_{L\alpha}\cos(\mu)qs & -\tan(\mu)\cos(\gamma)mg \\ \frac{T_\delta \sin(\mu)\sin(\alpha)}{\cos(\gamma)} & \frac{C_{L\alpha}\sin(\mu)qs}{\cos(\gamma)} & mg \end{pmatrix} \tag{3.9}$$

By equating $\dot{\mathbf{v}} = v_v$ where the pseudo-control v_v is given by a PID controller as follows:

$$v_v = K_v(v_c - v_m) + K_i(\int (v_c - v_m)) + K_d(\frac{d}{dt}(v_c - v_m)) \tag{3.10}$$

Equation 3.8 can, thus, be rewritten as:

$$K_v(v_c - v_m) + K_i(\int (v_c - v_m)) + K_d(\frac{d}{dt}(v_c - v_m)) = \dot{\mathbf{v}}_\mathbf{0} + B_v \begin{pmatrix} \Delta\delta \\ \Delta\alpha \\ \Delta\mu \end{pmatrix} \tag{3.11}$$

At every computation time step, the local linearization point $\dot{\mathbf{v}}_\mathbf{0}$ is evaluated through acceleration measurements.

- $\dot{V_{a0}} = a_x - g_x$
- $\dot{\gamma_0} = \frac{1}{V_{a0}}[a_z - g_z]$
- $\dot{\chi_0} = \frac{1}{V_{a0}} a_y$

where a_x, a_y and a_z are the measurements of the IMU in the body frame axes and g_x and g_z are the components of the gravity in the longitudinal and vertical directions of the path coordinate frame respectively.

Therefore, solving for the control variable ($\Delta\delta_f \;\; \Delta\alpha \;\; \Delta\mu$) :

$$\begin{pmatrix} \Delta\delta_f \\ \Delta\alpha \\ \Delta\mu \end{pmatrix} = B_v^{-1} \left[v_v - \frac{1}{V_{a,0}} \begin{pmatrix} V_{a0}(a_x - g_x) \\ a_z - g_z \\ a_y \end{pmatrix} \right] \tag{3.12}$$

d) **Position control**:

The goal of the position control loop is to minimize the deviation of the current flight position from a predefined reference path, which involves path angles γ_{ref} and χ_{ref}. The dynamics of this deviation in the lateral and vertical directions are determined by the translational kinematics equation 2.26. Importantly, these equations are independent of model-specific parameters, making it unnecessary to implement an incremental control concept in this loop.

Considering that both the commanded angles and angle deviations are small, and by applying small angle approximations, eq. 2.26 is further simplified into :

$$\dot{x_\Delta} = \begin{pmatrix} \dot{y_\Delta} \\ \dot{z_\Delta} \end{pmatrix} = V_k \begin{pmatrix} \chi - \chi_r \\ -(\gamma - \gamma_r) \end{pmatrix} \tag{3.13}$$

The right-hand side of equation 3.13 is treated as a pseudo control variable denoted by v_x and used to establish a linear system represented by $\dot{x_\Delta} = v_x$. The behavior of this pseudo-control is designed to follow that of a first-order system:

$$v_x = K_x x_\Delta \quad with \;\; K_x = \begin{pmatrix} k_y \\ k_z \end{pmatrix} \tag{3.14}$$

Combining equations3.13 and 3.14 and solving for the actual control vector:

$$\begin{pmatrix} \chi_c \\ \gamma_c \end{pmatrix} = \frac{K_x}{V_k} \begin{pmatrix} \chi - \chi_r \\ -(\gamma - \gamma_r) \end{pmatrix} + \begin{pmatrix} \chi_r \\ \gamma_r \end{pmatrix} \tag{3.15}$$

Despite the time-variant nature of the control matrix K_x resulting from dividing the control gain by the ground speed, it is assumed to be constant. This approximation is considered justified because the commanded velocity remains constant, leading to $\dot{V_k} \approx 0$.

3.2.2 Control modes

In order to enhance the control strategy's efficiency and facilitate direct input commands for the actuators, each aircraft flight is associated with a specific control mode. The controller can opt to use either the direct values provided by the guidance logic or the systematically calculated values for each control variable, as necessary.

The concept of control modes can be explained as follows: It is depicted by a three-element vector, where the first element represents the longitudinal mode, the second element denotes the lateral mode, and the third element gives the vertical mode. In terms of actuators, we utilize thrust for the longitudinal direction, rudder and aileron for the lateral direction, and elevator for the vertical direction. Regarding the control variables, we consider the speed V in the longitudinal direction, the azimuth χ and either the heading angle ψ or the side-slip angle β in the lateral direction, and both the flight path angle γ and the pitch angle θ in the vertical direction. In the following, the control modes corresponding to each direction are provided. Each mode will be briefly described, and their potential combinations will be explored.

- **Longitudinal direction** :

Mode	**Index**
Direct thrust command	11
Speed command	12

  The concept of the direct thrust command entails disregarding the commanded value provided by the control law and instead utilizing the value directly supplied by the guidance block. This is particularly useful in situations where commanding full thrust is necessary, such as during an emergency climb, or when no thrust is required due to an issue and the aircraft's acceleration needs to be halted. Conversely, the direct speed command provides the controller with the desired speed reference to be followed.

- **Lateral direction**:

Mode	**Index**
Direct aileron command	11
Direct rudder command	12
Direct aileron and rudder commands	13
Coordinated flight (β reference)	21
Heading tracking (ψ reference)	22
Track reference (χ reference)	23
Direct rudder command and track reference	24

As mentioned previously, the direct aileron and direct rudder commands involve bypassing the calculated commanded values and instead using those provided by the guidance block. It is important to note that during taxi and ground acceleration, aileron effectiveness is minimal due to the low speed and can be easily counterbalanced by the forces from the landing gear and ground. Therefore, there is no need for aileron actuation, and a neutral aileron command can be employed.

Additionally, when the aircraft is on the ground, the path azimuth/track χ and the aircraft's longitudinal axis/heading ψ always align. Consequently, by directing the nose wheel in the desired direction, the ground track can be followed. This is achieved by simultaneously actuating both the aileron and rudder (mode 13).

Moreover, the coordinated flight mode is useful for minimizing the side-slip angle by setting β (sideslip angle) to zero, which is crucial because flying in a slip is aerodynamically inefficient, resulting in a decreased lift-to-drag ratio. Consequently, a greater amount of drag is generated, consuming energy without producing sufficient lift.

Finally, the mode "Direct rudder command and track reference" is particularly beneficial during the flare/touchdown phase of the landing process, which will be discussed in detail in the subsequent section. The objective in this phase is to align the aircraft with the runway centerline and track the desired path, even in the presence of crosswinds.

- **Vertical direction**:

Mode	**Index**
Direct elevator command	11
rotation rate (q ref)	12
pitch angle (θ ref)	13
Flight path angle tracking (γ ref)	21

In general, when accelerating during takeoff, a downward elevator command can be used to angle the aircraft's nose slightly upwards. This maintains a positive angle of attack, which creates lift and keeps the aircraft in contact with the runway until the desired takeoff speed is achieved. Once this speed is reached, a rotation phase is initiated using a direct pitch rate (q) until the aircraft generates sufficient lift to become airborne. Furthermore, during the glideslope phase of the landing process, tracking a flight path angle reference provided by the guidance block proves particularly advantageous, as will be elaborated upon in the following section.

3.2.3 Automated Landing phases and challenges

The landing technique deployed in this paper closely resembles that employed by human pilots and comprises four distinct stages: the final approach, flare, touchdown, and ground phases. The primary difficulty in controlling the motion of an aircraft during automatic landing lies in the imbalance between the number of quantities that need to be regulated and the available actuators. Specifically, maintaining airspeed (V_A),the sink rate ($\dot{h} \approx \alpha$), and pitch angle (θ) within acceptable ranges with only two actuators, thrust and elevator. The system is under-actuated, which makes it impossible to achieve accurate values for all mentioned quantities in steady-state conditions. This implies that a compromise is required. Even though landings can still be achieved due to the interdependence of the three variables mentioned, the behavior of at least one variable will remain uncertain, making it a difficult control task. In the following, each phase is briefly explained, along with the corresponding variables to be managed. Additionally, the flare obstacle is outlined, and a proposed solution is presented.

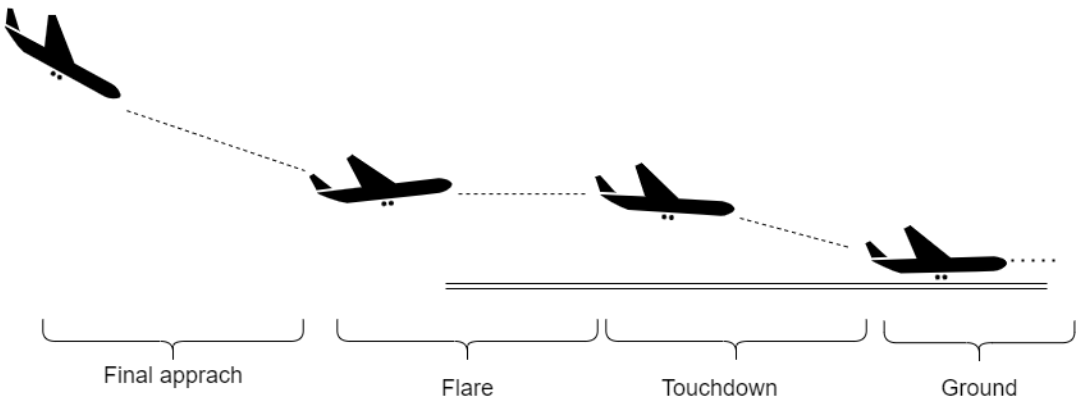

Figure 3.10: The landing process of a fixed-wing aircraft

a) **Final Approach:**

In this phase, the aircraft follows a flight path angle γ_{app} aligned with the runway direction. The controllable parameters during this stage are the velocity V_A and the flight path angle γ. At this point in the landing process, the aircraft remains at a relatively high altitude, and the pitch angle has minimal impact.

b) **Flare:**

Upon reaching a specific altitude above the ground, the flare maneuver is initiated to facilitate a smooth transition into landing. During this phase, the conflicting control goals regarding the values of θ, γ, and V_A are especially evident. The challenge, as previously mentioned, lies in limiting the three quantities - V_A, $\dot{h}$, and θ - within acceptable boundaries while using only the two actuators - thrust and elevator. By leveraging the interdependent nature of the three variables, it is possible to accomplish this task as will be explained below. However, it is important to consider that the precise value of the final velocity may not be explicitly known, but it can be controlled within an acceptable range to ensure that the aircraft maintains the desired landing attitude.

During this phase, an altitude command is implemented, following a predefined trajectory that gradually increases the path inclination angle through pitch movement. This trajectory aligns with the slope of the runway, enabling the aircraft to maintain a horizontal position at a consistent altitude above the runway. To simultaneously attain the desired values for both pitch angle (θ) and glide path angle (γ), it becomes necessary to reduce the excess velocity of the aircraft. This is achieved by setting a slightly negative command value for the rate of change of airspeed ($\dot{V_A}$), prolonging the glide-out process. Gradually, the velocity diminishes until the requisite pitch angle for touchdown is reached.

In order to improve tracking, it has been suggested to add feed-forward terms to control laws, as proposed in [14]. For the autopilot's landing trajectory, a polynomial height function based on the glide path angle γ_{app}, flare initiation altitude, and flare end altitude can be used. From this function, the value for γ can be derived and differentiated to achieve $\dot{\gamma}$ and through algebraic manipulation $\dot{\alpha}$ and $\dot{q}$. $\dot{\gamma}$ can then be added to the second term of the velocity control law 3.8, $\dot{\alpha}$ can be added to the second term of the attitude control law 3.7 and $\dot{q}$ to the rate control law 3.6 respectively. Implementing this modification has proven effective in improving the flight path angle tracking across various flare initiation altitudes and glide path angles, as demonstrated in the results section.

c) **Touchdown:**

In the subsequent touchdown phase, it is desirable for the aircraft to be in extremely close proximity to the ground. A negative commanded glide path angle $\gamma_{cmd} < 0$ is set and controlled through thrust actuation, while the pitch angle is maintained at a default value using the elevator. As a result, an uncertain velocity arises, influenced by the combination of angle of attack, inclination angle, environmental conditions, and aircraft aerodynamics.

d) **Ground:**

In the initial phase on the ground, a consistent pitch angle is maintained while the velocity is gradually reduced. Following this brief deceleration period, the final phase commences, where downward force is applied to the tail wheel for effective steering by pulling the elevator.

After touchdown with all wheels, it is crucial to maintain a stable pitch angle until the velocity has been adequately reduced. Thus, the control variables during this phase are represented by the velocity V_A and the pitch angle (θ).

4 Experimental setup and results:

4.1 Hardware setup

In order to test the cascaded INDI controller architecture and guidance algorithms proposed in earlier chapters, flight demonstrations were planned to be conducted using a modified version of the FunCub XL ND. This model was introduced earlier in Chapter 4 and has been altered to include an on-board autopilot system and various sensors. Additionally, it has been converted from a tail-wheel to a nose-wheel (refer to Figure 4.1).

Figure 4.1: FunCub model with a nose-wheel

The autopilot system implemented is the Pixhawk 4 on-board computer, which has been equipped with customized firmware based on the original PX4 Autopilot Repository on GitHub. This firmware has been modified by members of the Institute of Flight Mechanics and Control (IFR) to allow for easy hardware-in-the-loop simulations and the generation of code from the Simulink model.

Other equipment utilized during the demonstrations includes the IMU and GPS receiver with magnetometer, which are part of the standard Pixhawk equipment, along with an airspeed sensor and telemetry mounted to the aircraft. A customized navigation algorithm has been developed to estimate the aircraft's state (position,

velocity, attitude) based on the available sensors. All functional software is executed at a rate of 100 Hz.

Several software-in-the-loop simulated flight tests were conducted within the simulation environment of MATLAB/SIMULINK. However, the Hardware-in-the-loop testing and real-world flight tests of the physical aircraft were not completed due to time constraints in the research. In the upcoming section, the results obtained from the software-in-the-loop simulations are presented and discussed.

Within the simulation environment of MATLAB/SIMULINK, several software-in-the-loop simulated flight tests were conducted. However, due to time constraints in the research, the Hardware-in-the-loop testing and real-world flight tests of the physical aircraft were not completed.

4.2 Simulation results

To visualize the results, a state monitor block was employed to plot the aircraft's attitude. Additionally, multiple scopes and the Simulink 3D Animation viewer areoblk_HL20" were utilized to visualize the airframe.

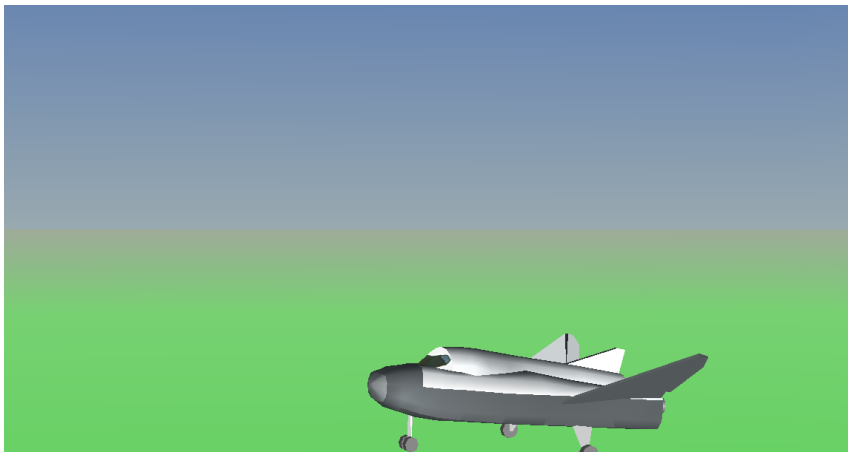

Figure 4.2: areoblk_HL20 Visualization

The figure below depicts a waypoint follower routine that initiates takeoff from point 1 on the ground and then cruises to point 5. It is clear that the aircraft can adeptly track the specified reference path.

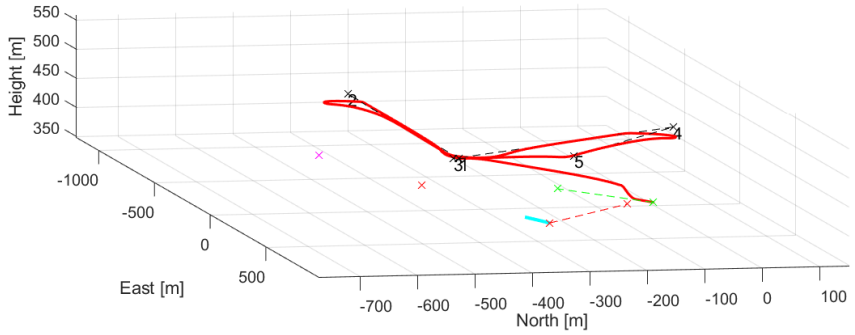

Figure 4.3: Waypoint follower routine

The process of takeoff and landing, along with a brief cruising phase in between, is shown in the recorded procedure depicted in Figure 4.5. Waypoint guidance techniques are used to complete the middle phase. Additionally, a chart displaying the different variables throughout the mission is included.

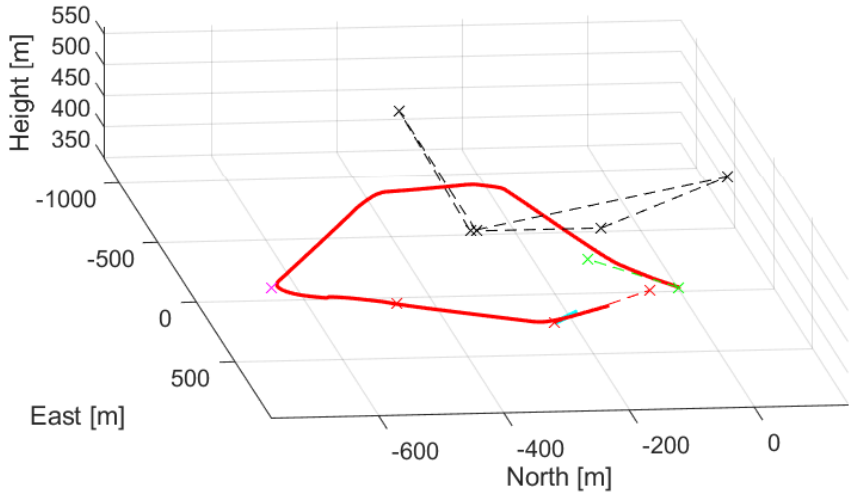

Figure 4.4: Simulation with entire ATOL mission

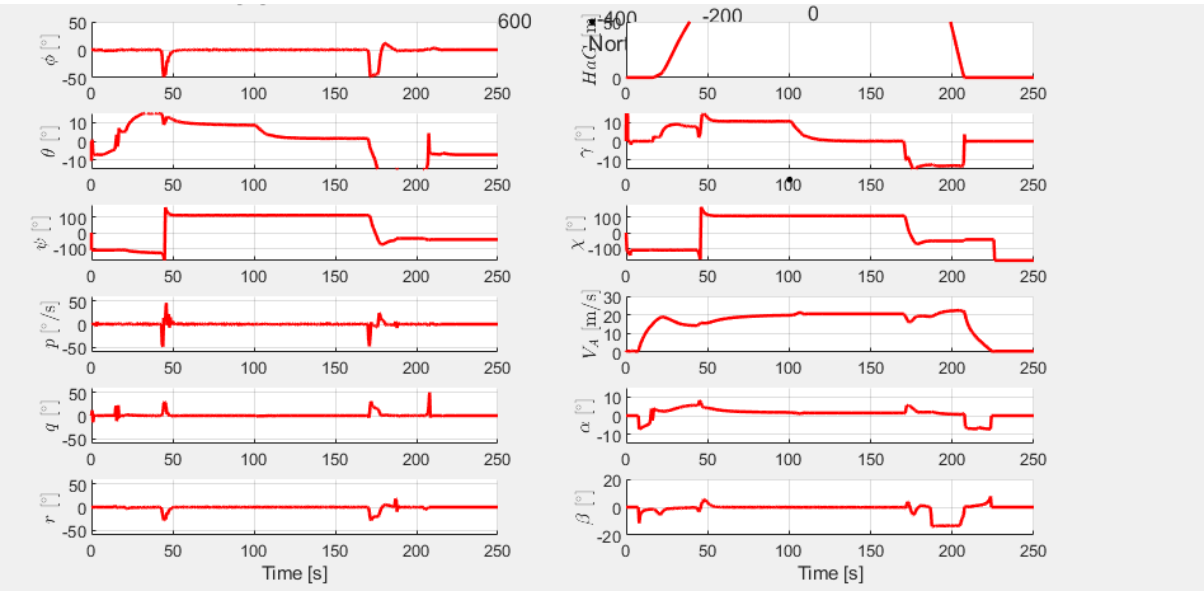

Figure 4.5: Plot of variables during ATOL

The impact of incorporating the feedforward terms on the flare process is showcased by comparing the reference nominal value of the flight path angle γ with the corresponding actual value of the signal. This assessment helps evaluate the accuracy of gamma tracking. Notably, the inclusion of the feedforward term enhances gamma tracking, as observed in the results.

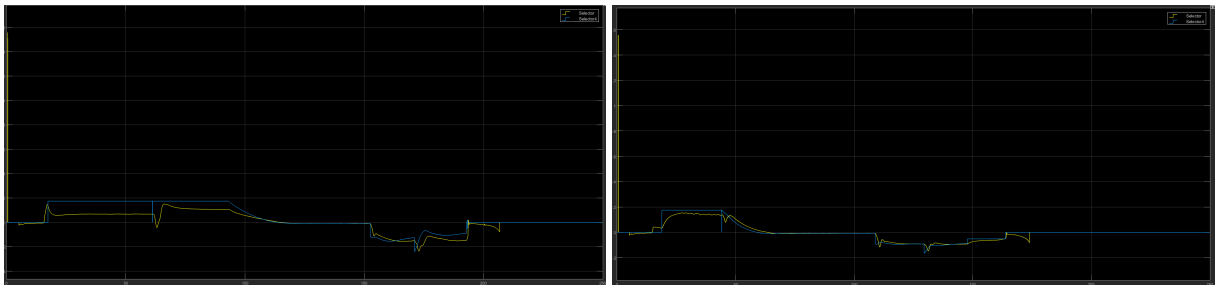

(a) Without feed-forward terms

(b) With feed-forward terms

The evaluation was conducted for various landing scenarios with varying Glide Path Angle (GPA) from 2 to 8 degrees and a height of flare trigger ranging from 15 to 2 meters. The findings indicated that even in challenging scenarios, there was no significant decline in the quality of the tracking.

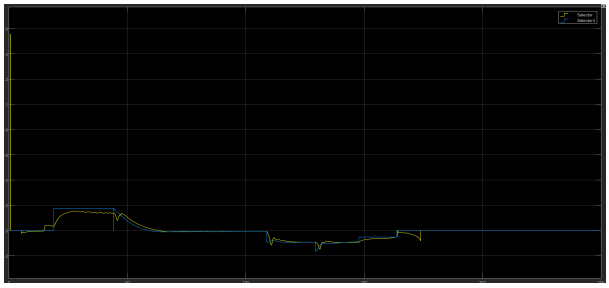

(a) GPA=-5 and H_{flare}=-15

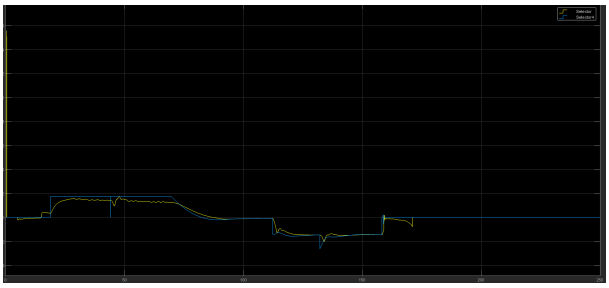

(b) GPA=-8 and H_{flare}=-2

4.2.1 Conclusion

This study demonstrates the successful implementation of an INDI-based flight controller for automated aircraft operations during landings, specifically tailored for nosewheel aircraft. The research highlights the substantial advantages of incremental control in terms of enhanced robustness and improved maneuver accuracy, especially in low-altitude flight. By incorporating feedforward terms, the gamma tracking during the flare phase of the landing process is significantly improved. The presented guidance and control concepts are rigorously validated through various flight simulations.

5 Summary and future work

5.1 Summary

This research explores the implementation of an Incremental Nonlinear Dynamic Inversion (INDI) flight controller for automated landings of fixed-wing tricycle gear unmanned aerial vehicles (UAVs). The study highlights the advantages of fixed-wing tricycle gear UAVs, such as efficient long-distance coverage and versatility in mission scenarios. The demand for UAVs in various applications necessitates improving their operational efficiency, reliability, and safety. Automated takeoff and landing procedures are crucial to achieving these goals, reducing human intervention, and enhancing operational capacity. Challenges related to environmental factors and ground effect affect the control effort required for precise state tracking. The study applies the INDI protocol, which reduces reliance on precise aircraft models and leverages translational and rotational accelerations measurements for robust control. The INDI control law is used for flight path and angular rate control loops, while the NDI control law is applied to position and attitude control loops. The research uses XFLR5 and MATLAB/SIMULINK for simulation and testing, and results demonstrate successful tracking and improvement with feed forward terms in the flare phase of landing. Overall, the proposed guidance and control concepts show promise for automated UAV operations, and the study provides a comprehensive analysis of the control system's capabilities.

5.2 Future work

The initial objective of this research included conducting a flight test campaign to obtain real-time in-flight data for the modeled airframe. This data would have been instrumental in validating and fine-tuning the simulation-based models to more accurately represent the performance and response of the target airframe. Unfortunately, due to time constraints, the flight test phase had to be reluctantly eliminated from the current research.

As a result, the next crucial step in advancing this research would be to pursue different validation approaches. Two prominent methods that can be employed are Hardware-in-the-loop (HIL) simulations and flight tests. HIL simulations involve

integrating the control algorithms with physical hardware components, such as actuators and sensors, within a controlled simulation environment. This approach allows for testing and refining the control system under realistic conditions, albeit in a controlled and safe setting.

Additionally, conducting flight tests with the actual physical aircraft remains an indispensable part of the validation process. These flight tests would provide empirical data, enabling a direct comparison with the simulated results and offering insights into the real-world behavior of the UAV during takeoff and landing operations.

In conclusion, future work should focus on the validation of the control system through HIL simulations and flight tests. This will ultimately pave the way for the successful implementation of automated takeoff and landing operations for the target airframe, contributing to the advancement of UAV technologies and their applications in various industries.

Bibliography

[1] https://academicflight.com/articles/kinematics/rotation-formalisms/euler-angles/

[2] Acquatella, B. P. ; Chu, Q. P.: Agile spacecraft attitude control: An incremental nonlinear dynamic inversion approach. In: *IFAC-PapersOnLine* 53 (2020), Nr. 2, S. 5709–5716

[3] Bakker, E. ; Nyborg, L. ; Pacejka, H. B.: Tyre modelling for use in vehicle dynamics studies. In: *SAE Transactions* (1987), S. 190–204

[4] Balas, G. J.: Flight control law design: An industry perspective. In: *European Journal of Control* 9 (2003), Nr. 2-3, S. 207–226

[5] Bauer, P. : A simple landing gear simulation model for unmanned aerial vehicles. In: *Periodica Polytechnica Transportation Engineering* 42 (2014), Nr. 1, S. 11–18

[6] Enns, D. ; Bugajski, D. ; Hendrick, R. ; Stein, G. : Dynamic inversion: an evolving methodology for flight control design. In: *International Journal of control* 59 (1994), Nr. 1, S. 71–91

[7] Hull, D. G. u. a.: *Fundamentals of airplane flight mechanics*. Bd. 19. Springer, 2007

[8] Johnson, W. : *Helicopter theory*. Courier Corporation, 2012

[9] Lu, P. ; Van Kampen, E.-J. ; De Visser, C. ; Chu, Q. : Aircraft fault-tolerant trajectory control using incremental nonlinear dynamic inversion. In: *Control Engineering Practice* 57 (2016), S. 126–141

[10] Nelson, R. C. u. a.: *Flight stability and automatic control*. Bd. 2. WCB/McGraw Hill New York, 1998

[11] Pfeifle, O. ; Fichter, W. : Cascaded Incremental Nonlinear Dynamic Inversion for Three-Dimensional Spline-Tracking with Wind Compensation. In: *Journal of Guidance, Control, and Dynamics* 44 (2021), 05, S. 1–13. http://dx.doi.org/10.2514/1.G005785. – DOI 10.2514/1.G005785

[12] Sieberling, S. ; Chu, Q. ; Mulder, J. : Robust flight control using incremental nonlinear dynamic inversion and angular acceleration prediction. In: *Journal of guidance, control, and dynamics* 33 (2010), Nr. 6, S. 1732–1742

[13] Slotine, J.-J. E. ; Li, W. u. a.: *Applied nonlinear control*. Prentice hall Englewood Cliffs, NJ, 1991

[14] Steinleitner, A. ; Frenzel, V. ; Pfeifle, O. ; Denzel, J. ; Fichter, W. : Automatic take-off and landing of tailwheel aircraft with incremental nonlinear dynamic inversion. In: *AIAA Scitech 2022 Forum*, 2022, S. 1228

[15] Stephan, J. ; Notter, S. ; Pfeifle, O. ; Pinchetti, F. ; Fichter, W. : Spline Trajectory Planning and Guidance for Fixed-Wing Drones. In: *AIAA Scitech 2020 Forum*, 2020, S. 0372

[16] Veld, R. van't: Incremental nonlinear dynamic inversion flight control: stability and robustness analysis and improvements. (2016)

[17] Wang, C. ; Holzapfel, F. : Modeling of the aircraft landing behavior for runway excursion and abnormal runway contact analysis. In: *2018 AIAA Modeling and Simulation Technologies Conference*, 2018, S. 1166